Chapter 3

Gold Nanostructures Prepared on Solid Surface

Jakub Siegel, Ondřej Kvítek, Zdeňka Kolská, Petr Slepička and Václav Švorčík

Additional information is available at the end of the chapter

http://dx.doi.org/10.5772/51617

1. Introduction

Up to now, many efforts have been made to produce smart materials with extraordinary properties usable in broad range of technological applications. In particular, within the last two decades, it has been demonstrated that properties of new prospective materials depend not only on their chemical composition but also on the dimensions of their building blocks which may consist of common materials [1,2].

A nanoparticle consists of a few atoms forming a cluster with size in the nanometer range. A nanometer represents a magical size of matter around which the vast majority of materials possess extraordinary, novel physico-chemical properties compared to its bulk form. Considerable attention has been focused during the last few decades on developing and optimizing methods for the preparation of gold nanoparticles to size and shape. Especially properties of 0D spherical and non-spherical particles, as applications of nanostructured materials, may differ considerably depending on the particle shape itself. Simple and straightforward example of the shape dependent behaviour of nanometer-sized particles is its colour. Ultrasmall gold spheres or clusters has been known for centuries as the deep red ruby colour of stained glass windows in cathedrals and domestic glassware. The colour results from the plasmon resonances in the metal cluster. Nowadays, most gold nanoparticles are produced via wet, chemical routes. Nevertheless, synthesis of metal nanoparticles (NPs) has been extensively studied since early 80's [3-9]. Some pioneering works on synthesis of gold nanoparticles were even published as far back as in early 50's by Turkevich [6]. Since that, many techniques have been developed, however, predominately based on wet, chemical processes [4-9]. Currently the most common noble-metal nanoparticle synthesis techniques are those developed by Brust-Shiffrin in 1994 [5]. The method based on reduction of Au^{III+} complex compound with $NaBH_4$ stabilized by thiols enables preparation of high stable particles with pretty narrow distribution and well-controlled size around 1 nm.

Besides interesting properties of nanostructured gold systems such as catalytic effects or magnetism [2,10], which both originate from surface and quantum size effects, they are also extremely usable those, which are closely connected with the average number of atoms in the nanoparticles. The properties and behavior of extremely small gold particles completely differ from those of bulk materials, e.g., their melting point [2,11,12], density [13], lattice parameter [13-15], and electrical or optical properties [13,14,16] are dramatically changed. Gold is also critical component in certain therapies, more specifically, in the treatment of cancer by hyperthermia and thermoablation. These two therapies use heat to kill cancer cells. In the case of hyperthermia, the cancerous tissue is heated to enhance conventional radiation and chemotherapy treatments, while in thermoablation the tissue is heated so that the cancer tissue is destroyed by the localised heat. In principle, there are two methods which can be used to provide heating, i.e. infra-red absorption and the application of an oscillating magnetic field to magnetic nanoparticles. Owing to this, nanosized gold is nowadays used in a vast range of cancer therapy applications such as cancer therapy agents [17] or cancer cell imaging [18,19]. Moreover, gold nanoparticles have often been conjugated with antibodies [20], or grafted to other carriers for surface property enhancement [21,22].

Besides above mentioned 0D nanostructures (nanodiscs, nanoparticles, nanoclusters) increasing efforts have been recently devoted also to one-dimensional (1D) nanostructures. 1D nanostructures in the form of wires, rods, belts and tubes have long been the focus of intensive research owing to their unique applications in mesoscopic physics and fabrication of nanoscale devices [23-25]. It is generally accepted that 1D nanostructures provide a good system for the investigation of the dependence of electrical and thermal transport or mechanical properties on dimensionality and size reduction (quantum confinement) [26]. Of the many elements and compounds from which nanowires may be made, gold is technologically important for its low electrical resistivity (2.21 μΩ cm) [27], its inertness to attack by air and its resistance to sulfur-based tarnishing [28]. Additionally, gold is more biocompatible than most metals, rendering it suitable for implantation [29,30] or electrical interfacing with cells [31,32] and tissues in nanobiological applications [33-35].

Nanostructured materials with high aspect ratios such as nanorods, nanowires, and nanoline patterns often exhibit anisotropic electronic and optical properties that differ from those observed in the bulk materials. These unique materials can be used to create many interesting devices, including fast responding chemical and biochemical sensors [36-40]. The high aspect ratio of nanowires should also make them interesting for the use in two dimensional photonic crystals, where vertical nanowires would constitute an array of high refractive index pillars in air [41]. Field emission from nanowires has also been reported [42], suggesting the possibility of devices such as field emission displays (FEDs) with nanowires acting as cathodes.

A variety of fabrication techniques have been developed in the past decade that yield high quality nanowires. Fabrication of ordered arrays of metallic nanoparticles supported on transparent substrate by sequential techniques like electron beam lithography has been demonstrated [43]. Such top-down approaches, however, are cumbersome and have a low

yield, which hinders practical applications. High throughput approaches for the synthesis of metallic nanowires are thus intensely searched [44-48]. In general, the production of arrays of nanostructures on substrates by lithographic techniques presents the disadvantage of high cost and a restriction in the number of materials to which it can be applied. The method can also prove to be complex and inefficient. Template based methods overcome those disadvantages, but the obtained structures often present a high number of imperfections due to packing defects in the original templates [49].

Above mentioned applications, however, usually require gold nanostructures (0D or 1D) to be either suspended in colloid solution or attached to another support medium. Concerning this, creation of nanostructured gold directly on appropriate support may be technologically valuable since one can avoid additional preparation step oriented on metal-substrate mutual attachment. Therefore, this chapter focuses on new possible approaches for nanostructuring of gold layers either formerly deposited on solid substrates (polymer or glass) or during deposition itself (polymer). The formerly mentioned technique is based on the intensive post-deposition thermal annealing of sputtered layers on polytertaflouroethylene (PTFE) or glass, whereas the latter technique is based on forced (preferential) growth of gold on nanostructured polymer template. The method, combining nanoscale patterning of the polyethyleneterephtalate (PET) substrate by polarized light of excimer laser with glancing angle deposition of the gold, provides an interesting alternative to time consuming sequential lithography-based nanopatterning approaches.

First part of the text is focused on the study of selected physico-chemical properties of deposited gold layers and its changes induced by post-deposition annealing. The gold nanostructures of different thicknesses were sputtered onto glass or polymer (PTFE) substrate and then the samples were annealed from room temperature to 300°C. The effects of annealing on gold structures sputtered onto substrate, their surface morphology and roughness were studied using Atomic Force Microscopy (AFM), lattice parameter and crystallites size and their distribution by X-ray diffraction (XRD) and by SAXSess. Hall mobility, volume resistance and free carrier concentration were measured by Van der Pauw method, an electric permitivity by ellipsometry, an optical band gap by UV-Vis spectroscopy and a sheet resistance of gold nanostructures by 2-point method.

In the next part special attention will be given to the irradiation of PET surface with linearly polarized light of a pulsed KrF excimer laser to produce templates for preparation of laterally ordered self-organized arrays of metallic nanowires. Different fluences and angles of incidence of the laser beam were applied. The periodicity of the ripples created on the polymer surface was controlled by changing the incidence angle of laser light during irradiation. Subsequently the modified polymer surface was coated with gold using two deposition techniques (sputtering and evaporation). The surface of nano-patterned coated/uncoated PET was analyzed by AFM and a scanning electron microscopy equipped with a focused ion beam (FIB-SEM), allowing to cut cross-sections of the laser patterned substrate surface and the deposited gold layers

2. Gold nanostructures on glass substrate

An overview of growth process, morphology, electrical and optical properties of ultra-thin gold layers sputtered on glass is provided in following sections. Insight into the phenomena taking place during post-deposition thermal treatment is also given.

2.1. Thickness, morphology and inner structure

Thickness of sputtered layers was measured by AFM. Thickness in the initial stage of deposition (sputtering time less than 50 s) was determined from the SEM image of the sample cross-section (FIB-SEM). Dependence of the layer thickness on sputtering time is shown in Fig. 1. Linear dependence between sputtering time and structure thickness is evident even in the initial stage of the layer growth. This finding is in contradiction with results obtained earlier for Au sputtering on PET [50]. In that case, the initial stage of the layer growth was related to lower deposition rate which is due to different morphology.

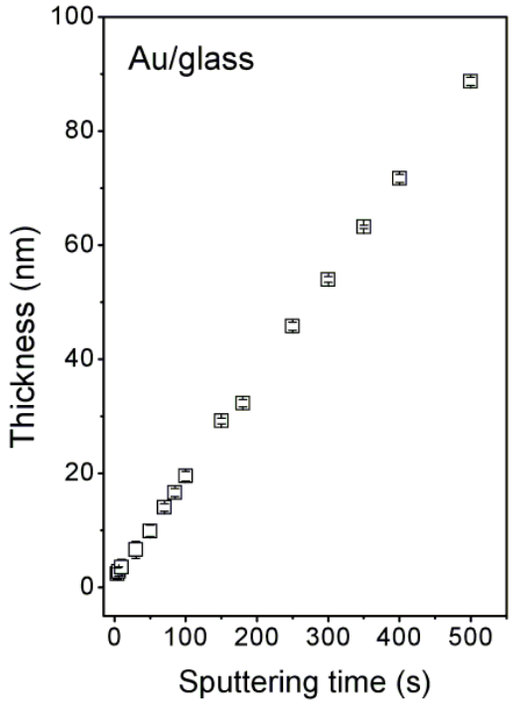

Figure 1. Dependence of the gold structure thickness on sputtering time [13].

In Fig. 2, a SEM picture of the cross-section of the Au layer at its initial stage of growth is shown. It is obvious that after approximately 20 s of Au deposition, flat, discrete Au islands (clusters) appear on the substrate surface. The flatness may indicate preferential growth of gold clusters in a lateral direction. When the surface coverage increases and the clusters get in close contact with each other, a coarsening sets in and becomes the dominant process. After the surface is fully covered, additional adsorption causes only the vertical layer growth, while the lateral growth is dominated by cluster boundary motion [51].

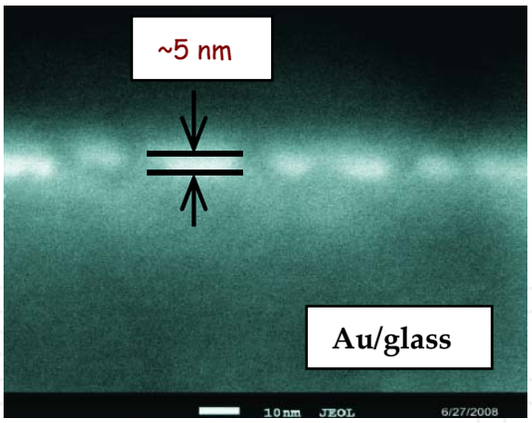

Figure 2. SEM scan of the FIB section of gold structure on glass substrate. Deposition time was 20 s. [13].

The AFM images that illustrate the surface morphology and roughness (R_a) of gold-coated glass before and after annealing are shown in Fig. 3. For the sake of comparison only images of the samples with identical vertical scale were chosen. From Fig. 3 it is clear that the surface morphology of the as-sputtered structures does not depend significantly on the sputtering times. Monotonous decrease of surface roughness with deposition time is related to the stage of the layer growth. During initial stages of metal growth the layer is formed over isolated islands. After that, during ongoing deposition, interconnections between clusters are formed and the deposited layers become homogeneous and uniform. Decrease of surface roughness is direct evidence of the formation of a thicker layer during sputtering process on flat substrate. After annealing, however, the surface morphology changes dramatically. Similar changes in the morphology of the thin gold structures have also been observed on the samples annealed at 200°C for 20 hours [52] and at 450°C for 2 hours [11]. It is seen from Fig. 3 that the annealing leads to the formation of "spherolytic and hummock-like" structures in the gold layers. The formation may be connected with an enhanced diffusion of gold particles at elevated temperature and their aggregation into larger structures. It is well known that the melting point of the gold nanoparticles decreases rapidly with decreasing particle size [2,11,12].

The migration of the gold nanoparticles and formation of larger structures may be connected with lower thermodynamic stability of the gold nanoparticles and lower gold wettability of glass. This idea is supported by some previous XRD experiments in which dominant (111) orientation of gold crystals in the sputtered gold layers was determined [11, 53]. The (111) oriented gold crystals are known to be thermodynamically unstable and their melting and cracking starts from the edge parts that should be bounded to Au (110) surface [11].

Metallic nanoparticles and generally nanostructures composed of metals often exhibit different values of structure parameters compared to their bulk form e.g. contraction of lattice parameter in nanostructures increases material density [13,53]. Lattice parameters *a* of the face-centered cubic gold nanostructures determined before and after annealing are

shown in Fig. 4 as a function of the sputtering time (i.e. effective layer thickness). Lattice parameters were calculated using the Rietveld procedure (full pattern fitting). For this purpose the five strongest diffraction lines were taken into account. For very thin films the diffraction lines are weak and the resulting values of the lattice parameters are loaded by a higher error. The error is especially large for the as-sputtered samples. A dramatic difference is found in the dependences of the lattice parameter on the sputtering time between as-sputtered and annealed samples. For as-sputtered samples the lattice parameter varies rapidly with the increasing sputtering time, i.e. with the increasing mean size of the gold crystallites [16,53,54]. It is seen that a maximum lattice parameter is observed after 100 s of sputtering, i.e. for the layer thickness of about 18 nm. For both the thinner and thicker layers the lattice parameter declines significantly. The same trend in the lattice parameter vs. sputtering time dependence was reported also for silver structures, for which the lattice parameter increases slightly up to the structures size of 12 nm and then decreases [55]. In contrast to the as-sputtered gold structures at the annealed ones the lattice parameter is nearly independent on the sputtering time and the size of the structures.

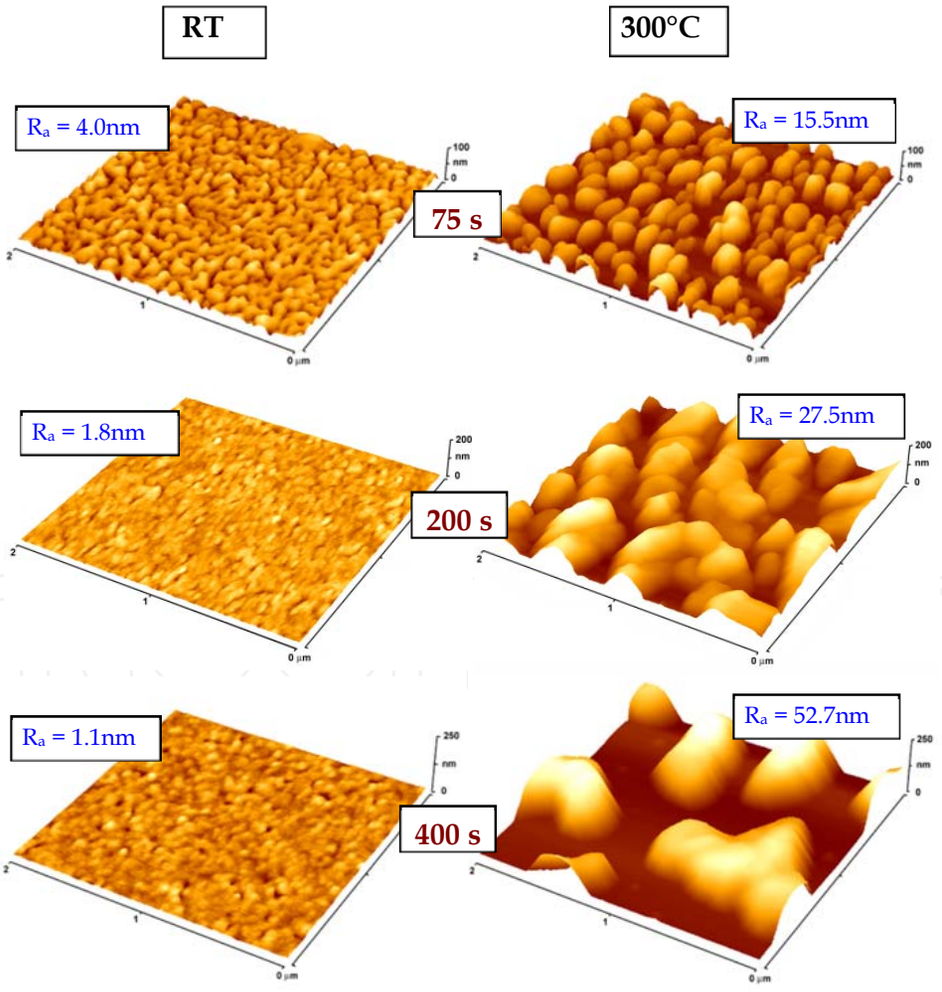

Figure 3. AFM scans of gold structures sputtered for 75, 200 and 400 s on glass substrate before (RT) and after annealing (300°C). R_a is the average surface roughness in nm [16].

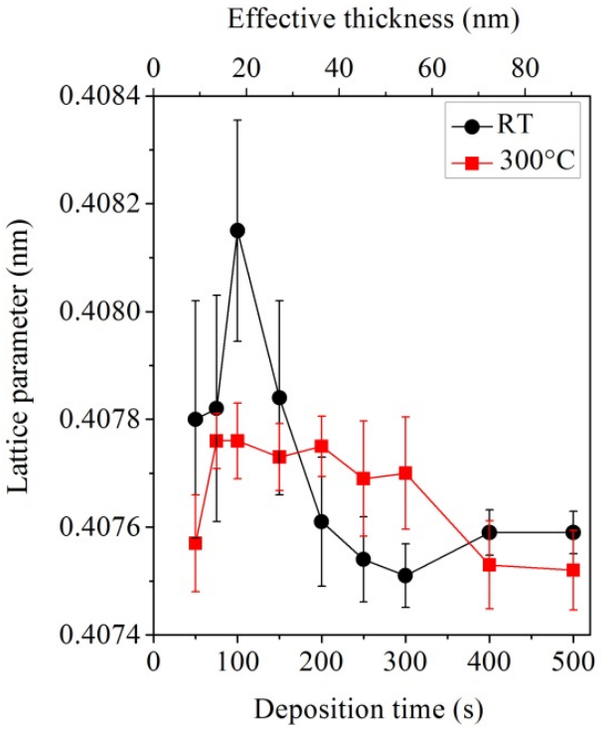

Figure 4. Dependence of the gold lattice parameter on the sputtering time (i.e. effective thickness) measured before (-●-) and after annealing at 300°C (-■-)[14].

The dependence of the crystallite size on the sputtering time before and after annealing is shown in Fig. 5. The dependences are quite different for the as-sputtered and annealed samples. While in the as-sputtered samples the crystallite size is amonotonously increasing function of the sputtering time, in the annealed ones the crystallite size first increases rapidly up to the sputtering time of 250 s, achieves a maximum and then it decreases. A dramatic increase of the Au crystallite size with the annealing temperature was published also by Santos et al. [56].

Size distribution of the Au crystallites determined by SAXSess method is presented in Fig. 6. The mean crystallite size values (modus) determined by SAXSess (S) and by XRD (X) are compared in Fig. 5. It is obvious that before annealing both methods (SAXSess, XRD) give the same values of the mean crystallite size, which increase slightly with the deposition time. Both SAXSess and XRD measurements prove dramatic increase of the mean crystallite size after annealing. However, there is an obvious dissimilarity between SAXSess and XRD results regarding longer sputtering time which is caused by inability of the SAXSess method to examine crystallites larger than ca 90–100 nm. The different behavior may be due to a crystallites' re-crystallization in the annealing process. The crystallite size determined by the XRD technique is based on the determination of the so-called coherently diffracting domains with their mean dimensions in direction perpendicular to the film surface. This is the reason why the crystallites determined in this way significantly exceed their size in some cases.

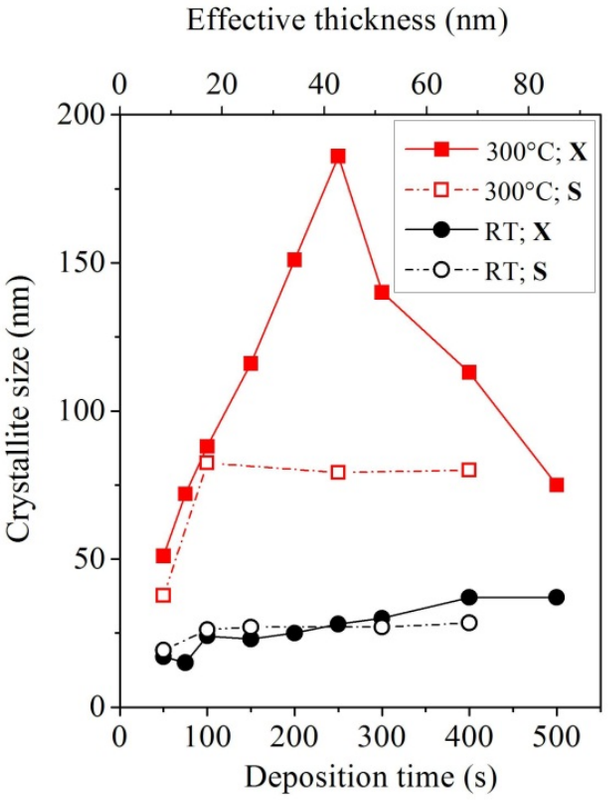

Figure 5. Dependence of the size of the gold crystallites on the sputtering time (i.e. layer effective thickness) measured before (-○S, -●- X) and after annealing at 300°C (-□- S, -■X) using S – SAXSess, X – XRD methods [14].

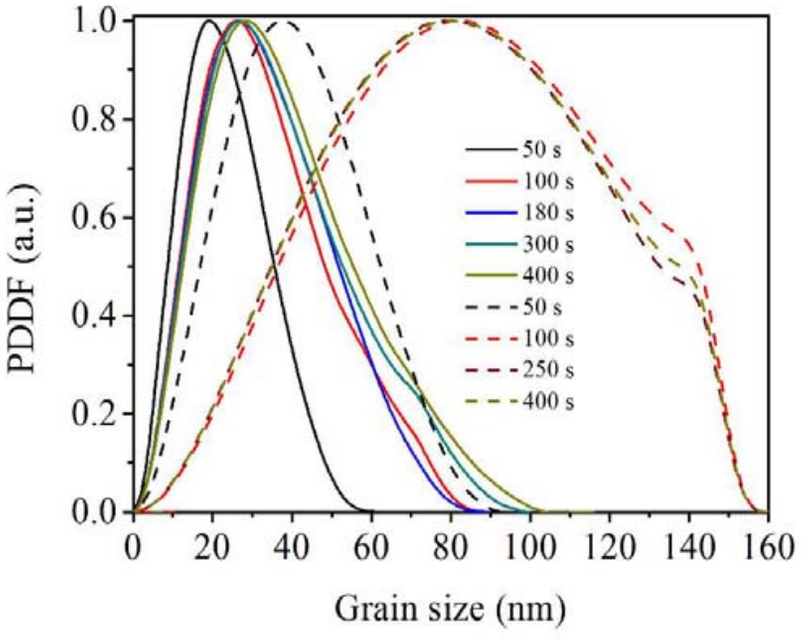

Figure 6. Pair distance distribution functions (PDDF) of gold crystallites by different sputtering time (in seconds) before (solid line) and after annealing (dashed line) measured by SAXSess method [14].

2.2. Optical and electrical properties

Besides interesting catalytic and electronic properties, nanoparticles of noble metals exhibit also distinctive, shape-dependent optical properties that have attracted great technological interest. This is particularly true for gold nanostructures [11]. Images of the sample surface for different sputtering times and for sputtered and annealed samples are shown in Fig. 7.

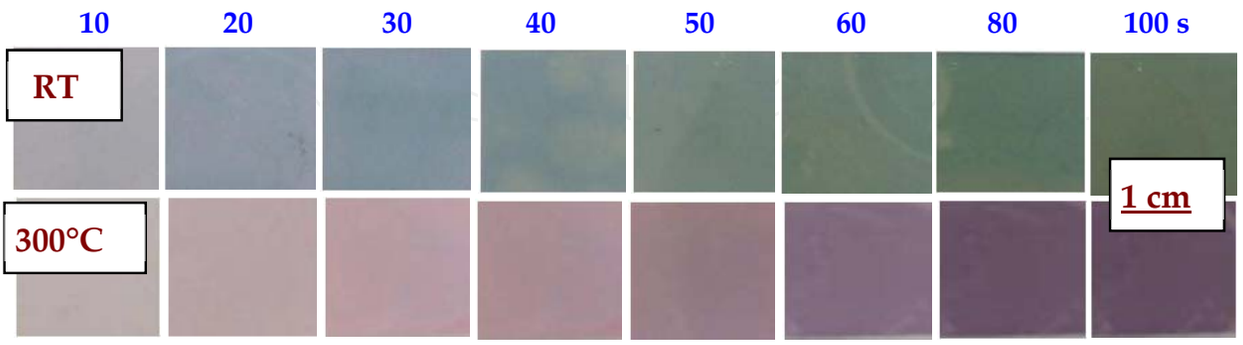

Figure 7. Images of the glass samples with gold structures sputtered for increasing times. The as-sputtered (RT) and annealed samples (300°C) are shown for comparison [16].

The deposited samples become darker with increasing sputtering time, the darkening being related to increasing thickness of the gold structures. Also a gradual change of the structures colour from blue to green is seen. After annealing all structures exhibit reddish colour, regardless of the sputtering time. The changes in the layer colour indicate pronounced alteration in the gold nanostructure caused by the annealing (see Fig. 3). It could be in accordance with previously presented results, the small gold sample about 10 nm absorbs green light and thus appears red [2]. This effect was confirmed also by UV-Vis spectroscopy. For the sake of clarity only some of UV-Vis spectra from as-sputtered and annealed samples are shown in Fig. 8 (RT and 300°C). The absorbance of gold structures increase with increasing sputtering time and structure thickness as could be expected. From comparison of the spectra of the sputtered and annealed samples it is seen that the annealed structures have qualitatively different shapes and lower absorbance. Both phenomena point at structural changes due to annealing. The observed shift of the 530 nm absorption peak (corresponding to surface plasmon resonance) with increasing sputtering time towards longer wavelengths is probably related to interconnection and mutual interaction of gold nanosized islands in the structure. From present UV-Vis spectra it is evident that the as-sputtered samples prepared for deposition time of 30 s and that annealed one (sputtering time 200 s) are the first ones, which do not exhibit the peak of plasmon resonance. Qualitative difference between absorbances of the sputtered structure and that annealed may indicate a transition from the structure comprising discrete gold islands to continuous gold coverage.

The UV-Vis spectra were also interpreted in the frame of the well-known Tauc's model [57] and the optical band gap (E_g^{opt}) was calculated as a function of the sputtering time for sputtered and annealed samples. This dependence is shown in Fig. 9. Also the gold

structure thickness vs. sputtering time measured by AFM method on the scratch step is presented. These values, inclusive the result that the AFM-scratch technique is not applicable on annealed structures due to their altered morphology, were taken from our previous work [53]. It is seen from Fig. 9 that the structures sputtered for times below 150 s exhibit non-zero E_g^{opt}. Rather dramatic change in the E_g^{opt} is observed after annealing, where the values of the E_g^{opt} are much higher in comparison with those of the sputtered sample. For samples sputtered for times around 300 s a non-zero E_g^{opt} is observed. For behaviour of ultra-thin metal structures (<10 nm) the surface-size and quantum-size effects must be considered [2,53,58]. This quantum-size effect in small structures leads e.g. to a semi-conducting character, which is accompanied by non-zero E_g (band gap) or E_g^{opt}. This effect was observed in the present case.

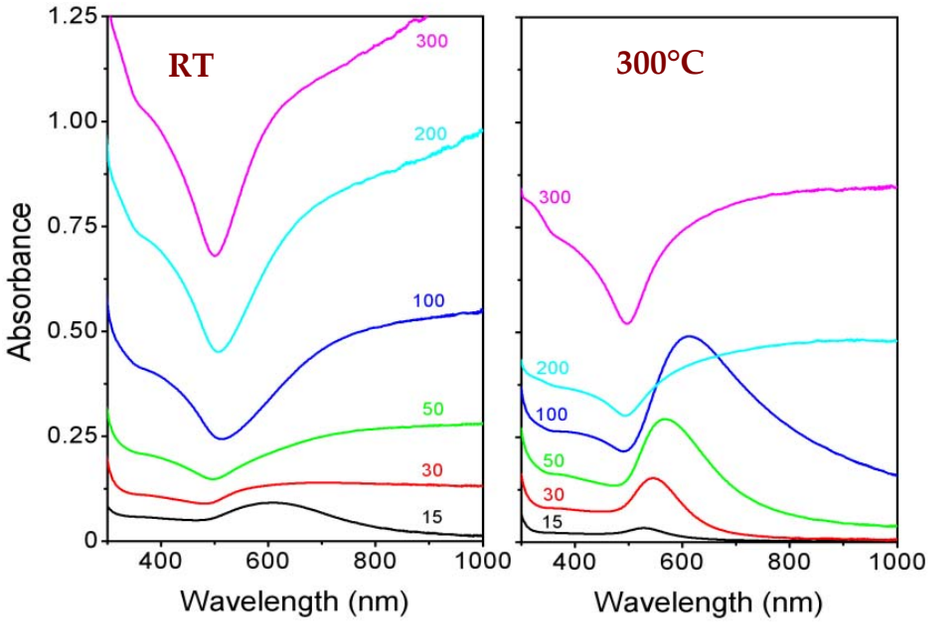

Figure 8. UV-Vis spectra of gold structures sputtered on glass before (RT) and after annealing (300°C). The numbers in Figs. are sputtering times in s [16].

The dependence of the volume resistivity on the sputtering time is seen from Fig. 10a. For as-sputtered samples a rapid drop of the resistivity over a narrow thickness interval is observed. The drop indicates a transition from electrically discontinuous to continuous gold coverage. For annealed samples the resistivity drop is shifted towards thicker layers. The difference is obviously connected with changes in the layer structure taking place during annealing i.e. gold coalescence and formation of isolated islands [16]. The onset of the rapid resistivity drop is observed after 50 and 150 s of sputtering for as-sputtered and annealed samples, respectively. Free carrier volume concentration and their Hall mobility significantly affect the electrical conductance of materials. The dependence of the free carrier concentration and the mobility on the sputtering time is shown in Figs. 10b and 10c, respectively. As can be seen from Fig. 10b, with increasing sputtering time the carrier

concentration increases dramatically and the layers become conductive (see Fig. 10a). As in the case of resistivity the onset of the rapid increase of the free carrier concentration on annealed samples is shifted towards longer sputtering time. Thus the constant level of the free carrier concentration is achieved later compared to the as-sputtered samples. A similar dependence of the free carrier concentration on the layer thickness was recently observed on PET and PTFE sputtered with gold [59]. The carrier mobility also changes dramatically with increasing sputtering time for non-annealed and annealed samples (Fig. 10c). The mobility first declines rapidly to a point when an electrically continuous layer is formed. The decline may be due to the fact that in a discontinuous layer the mobility mechanism differs from classical electron conductivity common in metals. For annealed structures the continuous layer is formed after a longer deposition time. For thicker, electrically continuous gold layers the mobility is a slowly increasing function of the sputtering time.

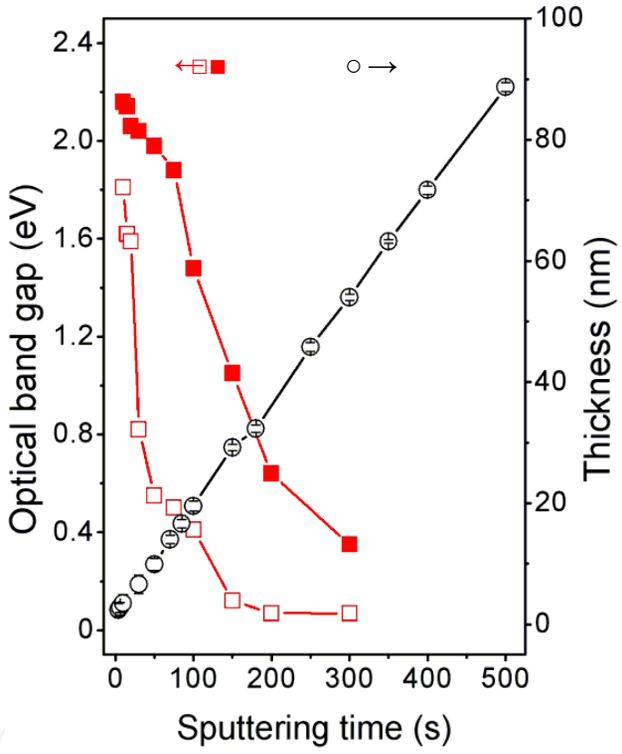

Figure 9. Dependence on the sputtering time of the optical band gap of gold structures before (RT) and after annealing (300°C) (-□- for RT and -■ for 300°C) and thickness (-○) [16].

There is a clear correspondence between mobility (Fig. 10c), free carrier volume concentration (Fig. 10b) and volume resistivity (Fig. 10a). A similar dependence of the free carrier concentration on the thickness of the gold layers deposited by sputtering on PET and PTFE was observed [59]. Simple and straightforward interpretation of the above described observations is that during electrical measurement on discontinuous gold layers an electron injection due to the tunneling effect occurs [13,16]. With ongoing deposition time the discrete structures become interconnected and form an electrically continuous, homogeneous layer in which the concentration of free carriers is saturated.

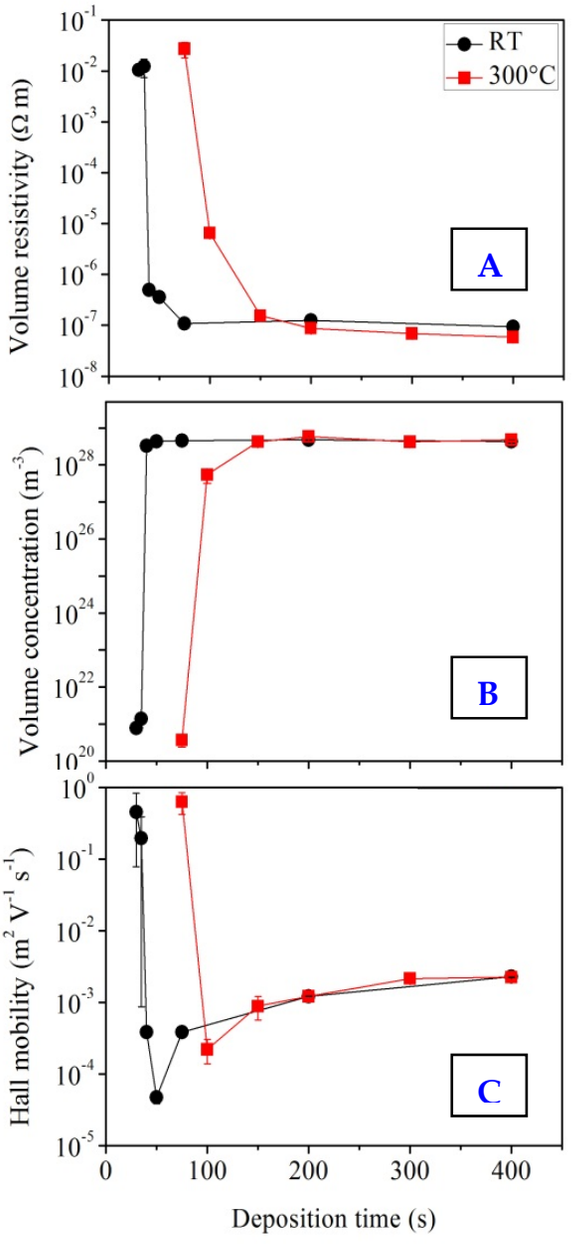

Figure 10. Dependence of the volume resistivity (A), surface free carrier volume concentration (B) and surface free carrier Hall mobility (C) on the sputtering time measured by van der Pauw technique before (-●-) and after annealing at 300°C (-■) [14].

The IR part of optical constants of the as-deposited and annealed Au films determined from ellipsometry also supports the results of electrical transport measurements. Fig. 11 presents the real part of electric permittivity in the studied spectral range.

Spectroscopic features in the Drude (IR) region clearly show the tendency of Au films to lose their metallic behavior with decreasing thickness due to gold coalescence, leading to a layer discontinuity [16]. Film discontinuity of the as-deposited thin layers is a natural consequence of the mechanism of the layer growth. Percolation threshold is reached at the layer thickness of about 7 nm [60] corresponding to the deposition time of about 25 s in the

present case. Fig. 11 also shows that the strong change in the surface morphology induced by the annealing shifts the metal-to-insulator transition towards greater layer thicknesses (i.e. deposition times). The thickness variation of IR end of the real part of the electric permittivity spectra of annealed gold layers (positive value reaching the maximum and then passing through zero to negative values with increasing deposition times) is consistent with previous studies of metallic films around the percolation threshold [60]. For the annealed layers with sputtering times equal to or smaller than those corresponding to the metal-to-insulator transition, a strong signature of plasmons is expected in the VIS part of optical constants. This is documented in Fig. 12, where the spectral dependence of the imaginary part of the electric permittivity is shown.

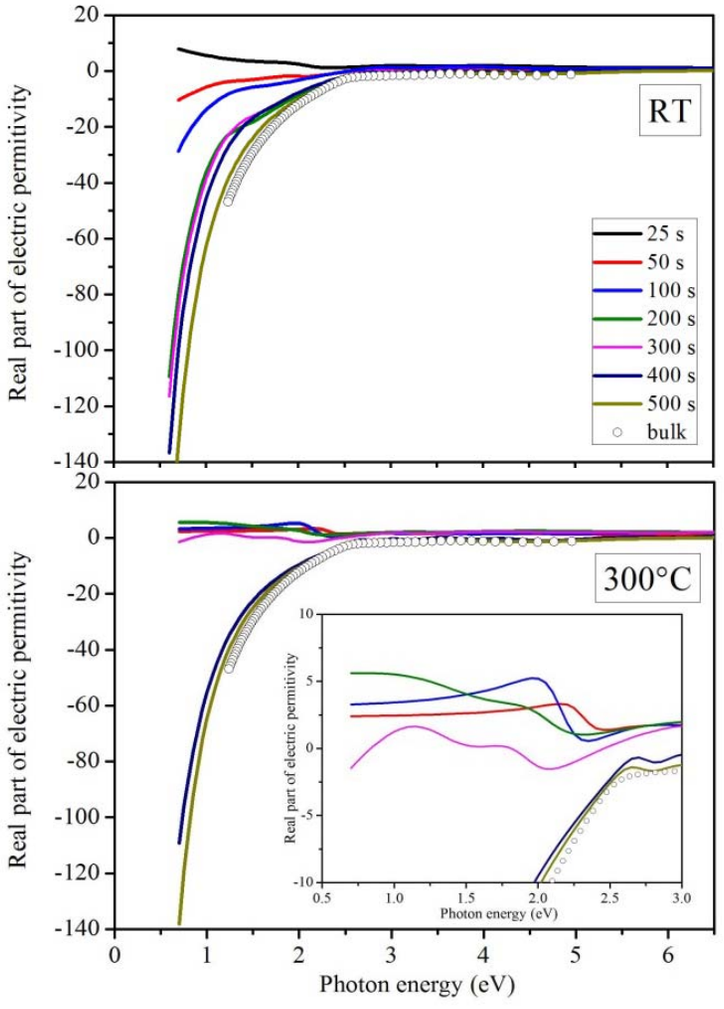

Figure 11. Real part of the electric permittivity spectra of as-sputtered (RT, upper part) and annealed (300°C, lower part) gold structures obtained by spectroscopic ellipsometry for the different sputtering times [14].

Plasmon oscillator band for the layer sputtered for 50 s is centered at around 2.3 eV (540 nm). With increasing deposition time the band becomes broader and shifts to longer wavelengths (lower photon energy). For 200 s sputtering time the plasmon band splits into two and for longer sputtering times it integrates into the Drude term in the IR spectral limit.

This change in the optical constants around the metal-to-insulator transition is the reason for the color variation of the annealed layers.

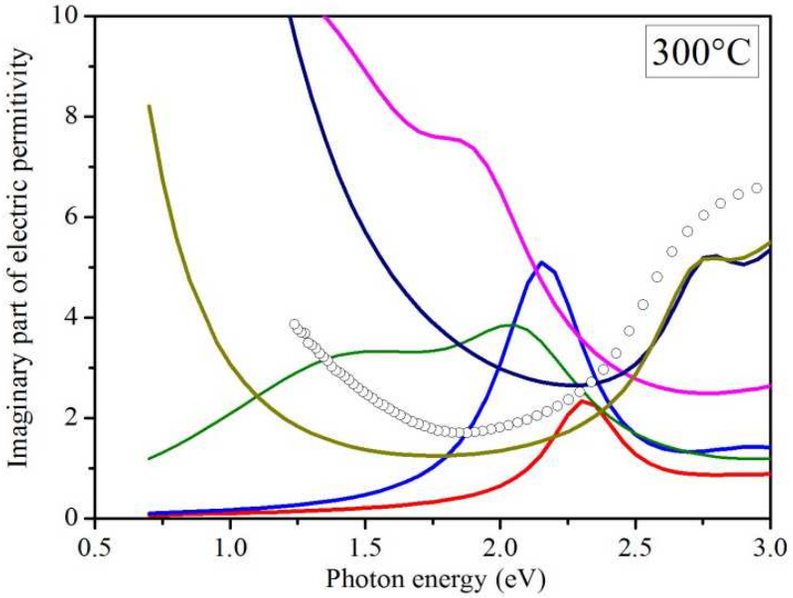

Figure 12. Imaginary part of the electric permitivity spectra of annealed (300°C) gold structures. The presence and evolution of the plasmon bands should be noted (for details see the text). Coloured sign of curves is the same as in Fig. 11 [14].

The temperature dependence of the sheet resistance for two particular structure thicknesses is displayed in Fig. 13. One can see that the temperature dependence of the sheet resistance strongly depends on the structure thickness. For the layer about 89 nm thick, the resistance is an increasing function of the sample temperature, the expected behavior for metals. For the structure about 6 nm thick, the sheet resistance first decreases rapidly with increasing temperature, but above a temperature of about 250 K, a slight increase in resistance is observed. The initial decrease and the final increase of the sheet resistance with increasing temperature are typical of semiconductors and metals, respectively. It has been referred elsewhere [2] that a small metal cluster can exhibit both metal and semiconductor characteristics just by varying the temperature. It is due to temperature-affected evolution of band gap and density of electron states in the systems containing low number of atoms.

From the present experimental data, it may be concluded that for the thicknesses above 10 nm, the sputtered gold layers exhibit metal conductivity. In the thickness range from 5 to 10 nm, the semiconductor-like and metal conductivities are observed at low and high temperatures, respectively. Our further measurements showed that the layers thinner than 5 nm exhibit a semiconductive-like characteristic in the whole investigated temperature scale. Except for band gap evolution theory, typical semiconductor-like behavior may also originate from the tunneling effect of electrons through the discontinuous, separated Au clusters during electrical measurements. Since the probability of electron tunneling depends on the temperature, similarly, typical course of sheet resistance and, as will be shown later, CV characteristic may be affected right by this phenomenon.

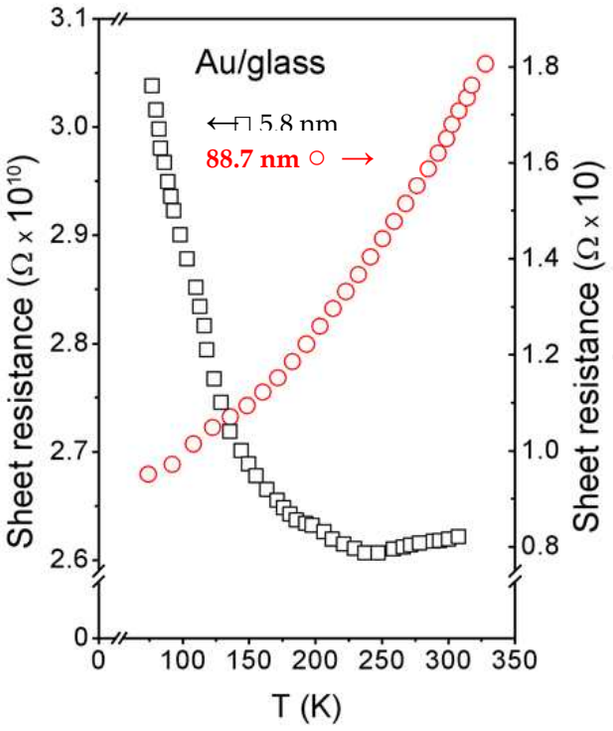

Figure 13. Temperature dependence of the sheet resistance for two different structure thicknesses indicated in the figure [13].

From presented measurements of sheet resistance results the semiconductor-like character of Au at specific structure conditions (thickness, temperature). The observed semiconductor-like character (decreasing resistance with increasing temperature) of ultrathin Au structures may originate from two undistinguishable phenomena. The first one results from a tunneling effect which occurs at discontinuous structures during resistance measurements [59]. The second one originates from the semiconductor characteristic of the intrinsic cluster itself, which occurs in metal nanostructures of sufficiently small proportions [2].

3. Gold nanostructures on polymeric substrate

In this section special attention is given to the changes in surface morphology and other physico-chemical properties of gold nanolayers, sputtered on polytetrafluoroethylene (PTFE) surface induced by post-deposition annealing.

3.1. Electrical properties

The dependence of the electrical sheet resistance (R_s) of the gold layer on its thickness before and after annealing (at 100, 200 and 300°C) is shown in Fig. 14. For the as-sputtered samples the sheet resistance decreases rapidly in the narrow thickness range from 10 to 15 nm when an electrically continuous gold coverage is formed. The resulting sheet resistance is saturated at a level of aproximately 200 Ω. From the measured R_s and effective layer thickness, layer resistivity R (Ohm centimeter) was calculated, which appears to be few

orders of magnitude higher than that reported for metallic bulk gold (R_{Au}^{bulk} = 2.5 × 10^{-6} Ω cm [61], e.g., for 100 nm thick Au layer $R_{Au}^{100\ nm}$ = 1 × 10^{-3} Ω cm). As in the case of Au coated glass substrate (see section 2), the higher resistivity of thin gold structures is due to the size effect in accord with the Matthiessen rule [62]. Annealing at temperatures below 200°C causes only mild shift in the resistance curve towards thicker layers. Transition from electrically discontinuous to electrically continuous layer in case of low temperature annealed samples is more gradual and occurs between the effective layer thicknesses from 10 to 20 nm regarding the annealing temperature. After annealing at 300°C a dramatic change in the resistance curve is observed. The annealed layers are electrically discontinuous up to the Au effective thickness of 70 nm above which the continuous coverage is created and a percolation limit is overcome. However, for longer sputtering times up to 550 s, the sheet resistance changes slowly and it achieves a saturation which is observed on the as-sputtered layers and layers annealed at low temperatures.

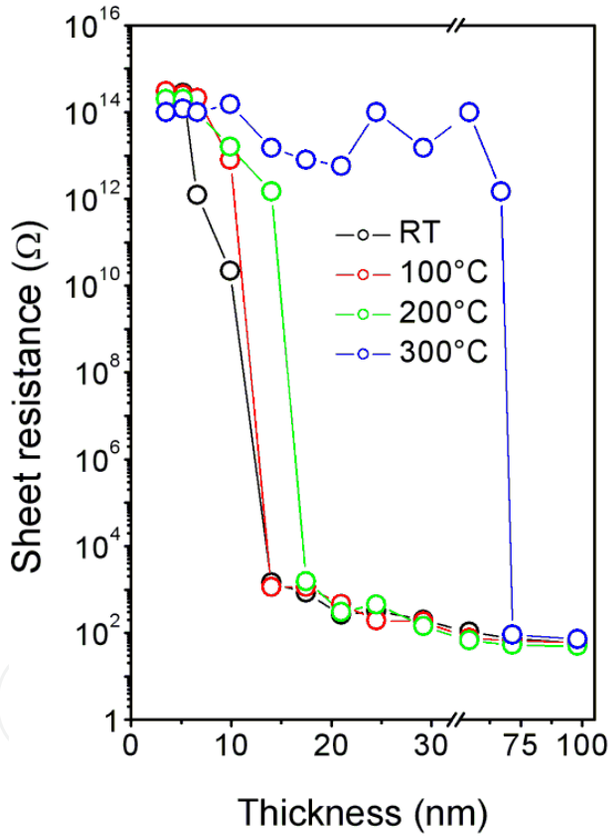

Figure 14. Dependence of the sheet resistance (R_s) on Au layer thickness for as-sputtered samples (RT) and the samples annealed at 100, 200 and 300°C [63].

Compared to electrical properties discussed in chapter 2 (Au layers on glass substrate), one can see that in case of PTFE substrate the transition from electrically discontinuous to continuous layer is shifted towards thicker layers. This fact is due to incomparable value of surface roughness of substrate used which is in the case of PTFE one order of magnitude higher (see section 3.3).

3.2. Chemical composition

Besides the sheet resistance measurements, information on the layer structure and homogeneity can be obtained in another way too. Here, complementary information on the layer homogeneity is obtained from XPS spectra. Fig. 15 A,B shows intensity normalized XPS spectra (line Au 4f) of 20 and 80 nm thick sputtered gold layers, respectively. Black line refers to as-sputtered layer and blue line to the one annealed at 300°C. Annealing of the 80 nm thick gold layer does not change the XPS spectrum. In contrast, the annealing of the 20 nm thick layer results in strong broadening of both lines which is due to the sample charging in the course of the XPS analysis. The charging is closely related to the change in the layer morphology: from electrically continuous one for as-sputtered sample to discontinuous one after the annealing procedure [16]. This observation is in agreement with above described results of the sheet resistance measurements (see Fig. 1, section 3.1).

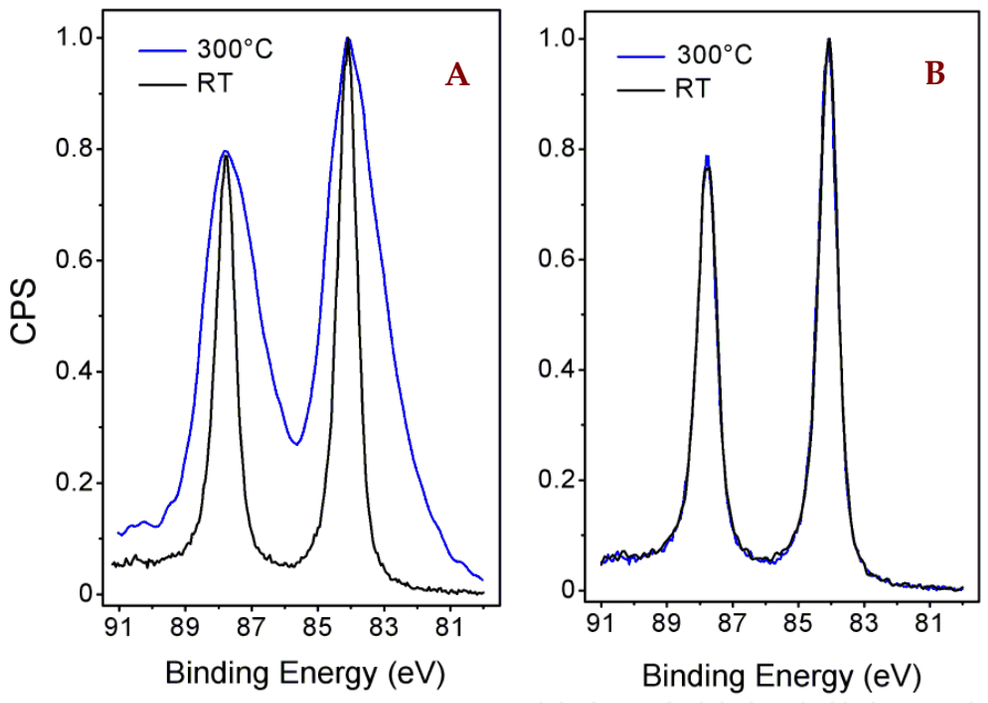

Figure 15. Intensity normalized XPS spectra (line Au (4f)) of 20 (A) and 80 nm (B) thick sputtered Au layers on PTFE before (black line) and after (blue line) annealing at 300°C [63].

Concentrations of chemical elements on the very sample surface (accessible depth of 6 to 8 atomic layers) determined from XPS spectra are summarized in Table 1. The XPS data were obtained for the samples with 20 and 80 nm thick gold layers, both as-sputtered and annealed at 300°C. Total carbon concentration and the carbon concentration coming from PTFE (calculated from XPS data) are shown in columns 1 and 2 of the table, respectively. Major part of the carbon is due to sample contamination. Fluorine to PTFE carbon ratio F/C^{PTFE} is close to that expected for PTFE (about 2). By the annealing at 300°C, the ratio decreases to 1.7 for both layer thicknesses. The decrease may be due to reorientation of polar

C-F groups induced by thermal treatment. Oxygen detected in the samples may result from oxygen incorporation during gold sputtering which may be accompanied by partial degradation and oxidation of PTFE macromolecular chain or degradation products. Subsequent annealing leads to reorientation of the oxidized groups toward the sample bulk and corresponding decrease of the surface concentration of oxygen. The same effects have been observed earlier on plasma-modified polyolefines [64]. It is also evident from Table 1 that annealing causes resorption of contamination carbon both hydrogenated and oxidized one [65]. Changes in the morphology of the gold layer after the annealing are manifested in changes of the gold and fluorine concentrations as observed in XPS spectra. After the annealing, the observed gold concentration decreases and fluorine concentration increases dramatically, these changes clearly indicate formation of isolated Au islands similar to those in case of Au-coated glass substrate [16].

Au layer Thickness	Temperature	Atomic concentrations of elements in at. %					
		C	C^{PTFE}	O	Au	F	F/C^{PTFE}
20 nm	RT	43.5	4.4	6.5	41.6	8.5	1.93
	300°C	37.8	34.8	0.4	3.4	58.4	1.68
80 nm	RT	41.0	3.1	4.4	48.6	6.0	1.94
	300°C	36.8	27.2	1.2	14.8	47.2	1.74

Table 1. Atomic concentrations (in at. %) of C (1s), O (1s), Au (4f) and F(1s) in Au sputtered PTFE samples with Au effective thickness 20 and 80 nm after deposition (RT) a after annealing (300°C) measured by XPS. C^{PTFE} represents calculated concentration from XPS data of carbon (in at. %) originating from PTFE only, F/C^{PTFE} stands for fluorine to PTFE carbon ratio [63].

3.3. Surface properties and morphology

Another quantity characterizing the structure of the sputtered gold layers is zeta potential determined from electrokinetic analysis. Dependence of zeta potential on the gold layer thickness for as-sputtered samples (RT) and annealed samples at 300°C is shown in Fig. 16. For as-sputtered samples and very thin gold layers, the zeta potential is close to that of pristine PTFE due to the discontinuous gold coverage since the PTFE surface plays dominant role in zeta potential value. Then, for thicker layers, where the gold coverage prevails over the original substrate surface, the zeta potential decreases rapidly and for the thicknesses above 20 nm remains nearly unchanged, indicating total coverage of original substrate by gold. For annealed samples, the dependence on the layer thickness is quite different. It is seen that the annealing leads to a significant increase of the zeta potential for very thin layers. This increase may be due to thermal degradation of the PTFE accompanied by production of excessive polar groups on the polymer surface, which plays the important role when the gold coverage is discontinuous. Moreover, the surface roughness increases at this moment too (see Table 1 and Fig. 17 below) [66]. Then, for medium thicknesses, ranging from 20 to 70 nm, the zeta potential remains unchanged and finally it decreases again for higher thicknesses due to the formation of continuous gold coverage. It appears that the results of electrokinetic analysis (Fig. 16) and measurement of the sheet resistance (Fig. 13) are highly correlated.

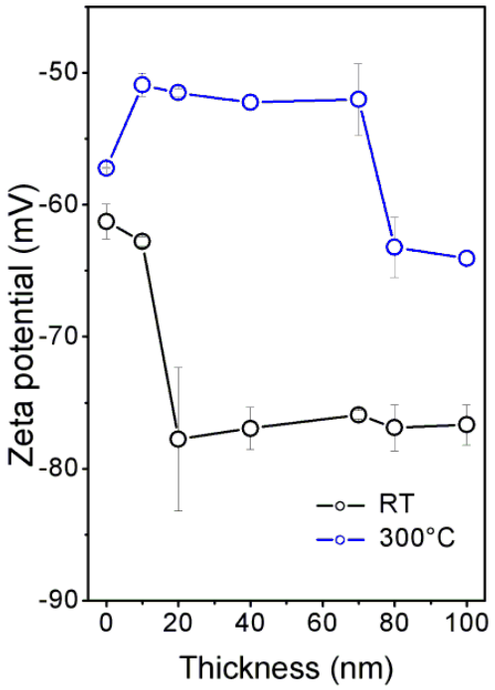

Figure 16. Dependence of zeta potential on the Au layer thickness for as-sputtered samples (RT) and the samples annealed at 300°C [63].

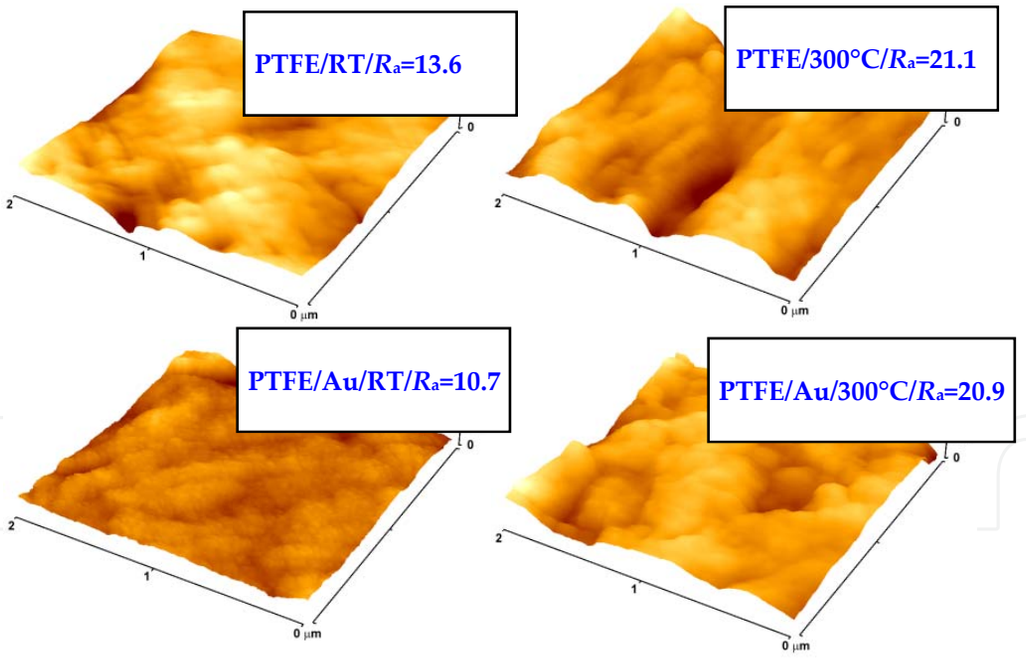

Figure 17. AFM images of pristine (PTFE) and Au coated (PTFE/Au) samples (thickness of 20 nm) before (RT) and after annealing at 300°C. Numbers in frames are measured surface roughnesses R_a in nm [63].

The rapid decrease in the sheet resistance occurs at the same layer thickness as the decrease in zeta potential. Both correlated changes are connected with creation of continuous, conductive gold coverage. Another interesting fact is that even for the layers with

thicknesses above 80 nm, the values of the zeta potential measured on as-sputtered and annealed samples differ significantly. This can be due to higher fluorine concentration in the annealed samples and the fact that the C-F bond is more polar and exhibits higher wettability. It should be also noted that the value of the zeta potential may be affected by the surface roughness too. In general, it follows that the thicker the gold coverage the lower the zeta potential is, reflecting the electrokinetic potencial of metal itself.

The changes in the surface morphology after the annealing were studied by AFM. AFM scans of pristine and Au-coated (20 nm) samples before and after annealing are presented in Fig. 17. One can see that the annealing causes a dramatic increase in the surface roughness of the pristine polymer. Since the annealing temperature markedly exceeds PTFE glassy transformation temperature (T_g^{PTFE} = 126°C) the increase in the surface roughness is probably due to thermally induced changes of PTFE amorphous phase. The gold sputtering leads to a measurable reduction of the sample surface roughness. The reduction may be due to preferential gold growth in holes at the PTFE surface. Annealing of the gold-coated sample leads to significant increase of the surface roughness too. In this case, the increase is a result of both, the changes in the surface morphology of underlying PTFE and the changes in the morphology of the gold layer. After annealing, the surface roughness of pristine and gold-coated samples is practically the same. This finding is in contradiction with similar study accomplished on gold layers deposited on glass substrate [16]. Possible explanation of this fact probably lies in much better flatness of the glass substrate and in lower thermal stability of PTFE substrate during annealing.

4. Self-organized gold nanostructures

Purpose of this section lies in description of phenomena taking place during both interaction of polarized laser light with the surface of polymeric material and its subsequent coating by metal. It will be shown that modification of the polyethylenetherephtalate (PET) surface with linearly polarized light from pulsed KrF laser has a significant effect on the properties of subsequently deposited gold nanolayers and the choice of the deposition technique is crucial owing to the quality of prepared coatings.

4.1. Surface morphology and structure parameters

It has been shown [67] that by the KrF laser irradiation with several thousand of pulses a periodic ripple structure is formed at a PET surface for a fluence range from about 4.2 to 18.8 mJ·cm^{-2}. The ripples have a fluence-independent width Λ, which is given by the formula $\Lambda = \lambda/(1 - \sin(\theta))$, Eq. (1) [68], where λ is wavelength of a laser light used, n the effective refractive index of material, and θ the angle of incidence. Fig. 18 displays AFM images of pristine PET and PET irradiated at different laser fluences. The sample irradiated with the laser fluence of 3.4 mJ·cm^{-2} exhibits a rougher surface than the flat un-irradiated pristine PET. There is a noticeable modulation, although no ripple formation is visible. At higher laser fluences periodic ripple structures have developed in the irradiated area. At a laser fluence of 6.6 mJ·cm^{-2}, a regular and uniform coverage of the PET surface with ripples

is reached. These results are based on AFM measurements, as those shown in Fig. 18. There is a good correlation between height and surface roughness of ripples over the whole laser fluence range shown in the figure. Both parameters reach the maximum value at a fluence of 6.6 mJ·cm^{-2}, which corresponds to a ripple height of about 90 nm.

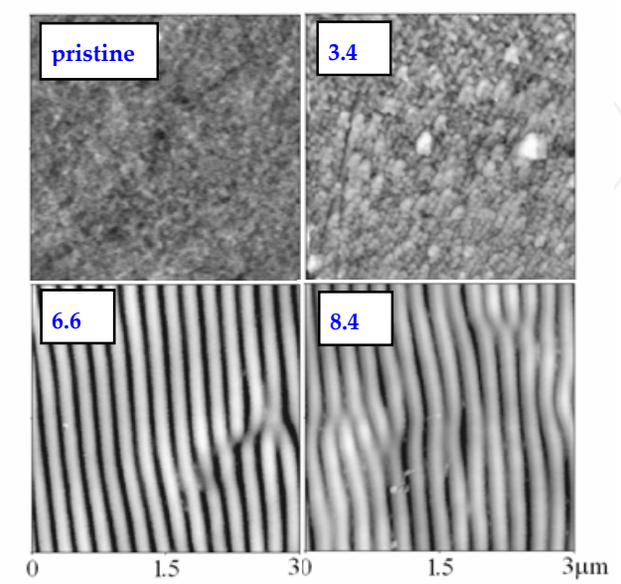

Figure 18. AFM images of the PET irradiated at different KrF laser fluences; the numbers in the inset refer to the laser fluence in mJ·cm^{-2} employed for irradiation of the PET foils, while pristine stands for unirradiated pristine PET [70].

The height and the roughness of the ripples as a function of the applied laser fluence are shown in Fig. 19.

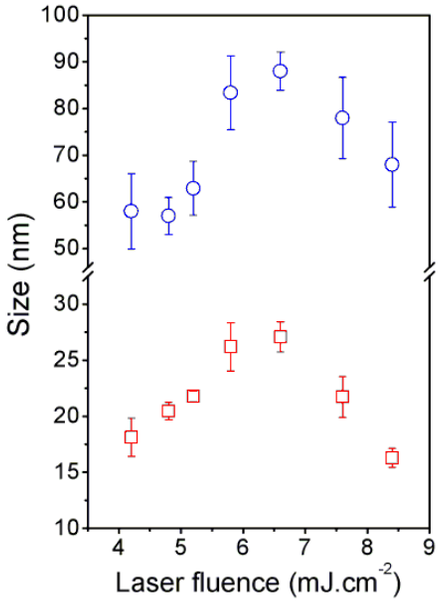

Figure 19. Dependence of the ripple height (○) and roughness (□) on the KrF laser fluence employed for the PET irradiation [70].

Fig. 20 shows AFM images of the PET irradiated under different incidence angles of the laser beam. For larger angles of incidence, the spacing between two neighboring ripples is wider. For the incidence angle of 0° and 22.5°, the observed spacing of the ripples is in good agreement with the value calculated by Eq. (1) with an effective index of refraction $n \approx 1.2$. The agreement for the incidence angle of 45° is less pronounced. The discrepancy may be due to changes of the polymer refractive index induced by the UV laser irradiation as reported earlier [69].

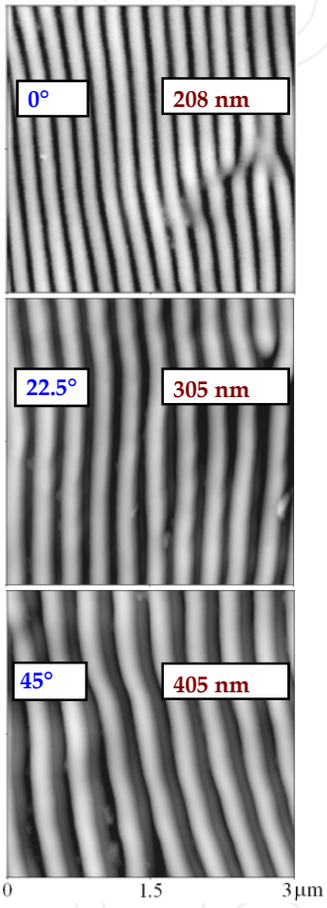

Figure 20. AFM images of the PET irradiated at a KrF laser fluence of 6.6 mJ·cm^{-2} under the different incidence angle of laser beam (0, 22.5 and 45°). The numbers in the insets in the upper left corner refer to the angle of incidence of the laser beam and in the insets in the upper right corner to the ripple period in nm [70].

FIB cuts of laser irradiated and gold coated PET samples were investigated by SEM (see Fig. 21). After sputtering, the gold is deposited in the form of "nanowires", which grow mainly at the ridges of the ripples. The FIB cuts reveal that there could be gaps between the individual wires and that the metal layer may be discontinuous. The width of the gold nanowires directly correlates to the width of the ripples formed before gold deposition. Additionally, a granularity is visible along the wires, but the FIB cut images suggest that the grains may be interconnected. The morphology of the gold layers deposited by evaporation is distinctly different. The gold is also deposited in the valleys of the ripple structure.

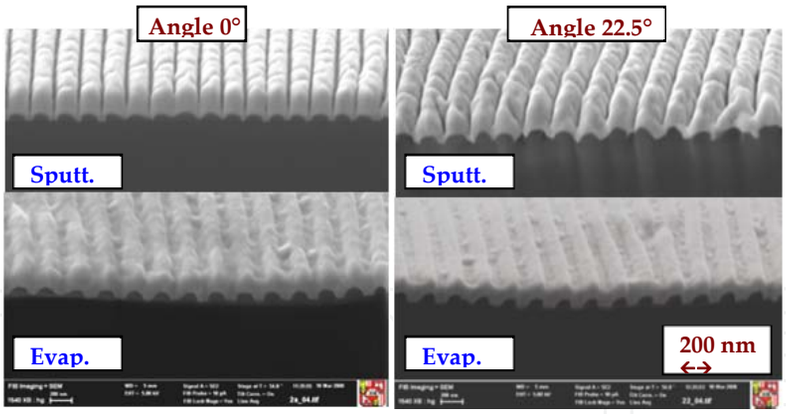

Figure 21. FIB-SEM images of the gold coatings on PET samples irradiated by a KrF laser under incidence angles 0 and 22.5° (fluence 6.6 mJ·cm^{-2}). The gold deposition was performed either by sputtering (Sputt.) and evaporation (Evap.) [70].

The nanowire structure of the sputtered gold layer can be observed also after gold deposition onto PET samples irradiated by the laser under an angle of incidence of 45°. Again, the evaporation of gold leads to a continuous coverage copying nanostructured polymer surface. The reason for the different observed gold morphologies after sputtering (nanowires) and evaporation (homogeneous gold coverage) is still unclear. The different particle energies in both processes are one possible reason. For sputtering, the particle energy may be considerably higher because of sample charging effect¸ while the evaporated materials should be slower (i.e., colder) and closer to thermodynamical equilibrium. The electrical charge of the sputtered particles can have also direct influence on layer formation, while the evaporated material should be mainly neutral. Other reasons may be the different deposition rates, which were a factor of two lower for sputtering than for evaporation, and possible differences of the substrate and gold layer temperature during the deposition in the two different techniques.

5. Summary

In summary, this chapter gives a comprehensive insight into the problematic of ultrathin gold films formed by physical deposition techniques on glass and polymeric substrates. Particular emphasis is given to the processes taking place during post-deposition annealing of prepared layers. In the case of glass substrate, the sputtering times and the layer effective thicknesses were chosen to span the region of the transition from discontinuous to continuous gold layer. For short sputtering times electrically discontinuous layers are obtained comprising discrete gold crystallites. The crystallite size in the as-sputtered samples is a monotonously increasing function of the sputtering time. The dependence of the lattice parameter of the gold crystallites forming the layer on the sputtering time is rather complicated with a rapid increase for shorter sputtering times and subsequent decrease for longer sputtering times. The decrease can be explained by relaxation processes in the thicker layers. The annealing has significant influence on the properties of the gold layers. For the annealed samples the lattice parameter practically does not depend on the

sputtering time. The crystallite size first increases rapidly up to the sputtering time of 250 s, achieves a maximum and then decreases. The electrical properties (concentration, mobility of charge carriers and volume resistivity) and NIR optical properties of the gold layers change dramatically as the function of the sputtering time. Other significant changes, especially for electrically discontinuous layers, are observed as a result of the annealing. This is probably due to the different mechanism of free charge carrier transport, where also the quantum surface effects could be present in case of observed island structure mainly after annealing. For electrically continuous layer the concentration and the mobility are invariable. Similar behaviour exhibits also gold layers on polymeric substrate. From the measurement of the sheet resistance the transition from discontinuous to continuous gold coverage was found at the layer thicknesses of 10-15 nm for as-sputtered samples. After annealing at 300°C the transition point increases to about 70 nm, the increase indicating substantial rearrangement of the gold layer. The rearrangement is confirmed also by XPS measurement and an electrokinetic analysis. By XPS measurement contamination of the gold coated PTFE samples with carbon and the presence of oxidized structures, created during gold sputtering were proved. The annealing results in significant increase of the surface roughness of both pristine and gold sputtered PTFE.

Modification of the PET surface with linearly polarized light from pulsed KrF laser has a significant effect on the properties of subsequently deposited gold nanolayers and the choice of the deposition technique is crucial owing to the quality of prepared coatings. Subsequent deposition of 200 nm thick gold layer caused a decrease of the surface roughness. While by evaporation a continuous metal coverage is formed, copying nanostructured polymer surface, in the case of sputtering a nanowire-like structure of the gold coating can be observed. It was shown that the width of the nanowires can be tailored by the width of the ripples formed by preceding laser irradiation. We demonstrate a technique for the controlled patterning of polymer surfaces, including the creation of nanopatterned, regular gold structures (nanowires). In principle, this technique could be employed for the creation of metal-polymer composites with interesting electrical, mechanical, and optical properties, which could find novel applications in micro and nanotechnology.

Author details

Jakub Siegel, Ondřej Kvítek, Petr Slepička and Václav Švorčík
Institute of Chemical Technology Prague, Czech Republic

Zdeňka Kolská
University of J.E. Purkyne Usti nad Labem, Czech Republic

Acknowledgement

Financial support of this work from the GACR projects No. P108/11/P337, P108/10/1106 and 106/09/0125 is gratefully acknowledged.

6. References

[1] Rao CNR, Kulkarni GU, Thomas PJ, Edwards PP (2002) Size-Dependent Chemistry: Properties of Nanocrystals. Chem. eur. j. 8: 25-39.

[2] Roduner E (2006) Size Matters: Why Nanomaterials are Different. Chem. soc. rev. 35: 583-592.

[3] Daniel MC, Astruc D (2004) Gold Nanoparticles: Assembly, Supramolecular Chemistry, Quantum-Size-Related Properties, and Applications Toward Biology, Catalysis, and Nanotechnology. Chem. rev. 104: 293-346.

[4] Guoa S, Wang E (2007) Synthesis and Electrochemical Applications of Gold Nanoparticles. Anal. chim. acta 598: 181-192.

[5] Yonezawa T, Kunitake T (1999) Preparation of Anionic Mercapto Ligand-Stabilized Gold Nanoparticles and their Immobilization. Colloid surf. A 149: 193-199.

[6] Turkevich J, Stevenson PC, Hillier J (1951) A Study of the Nucleation and Growth Processes in the Synthesis of Colloidal Gold. Discuss faraday soc. 11: 55-59.

[7] Kim HJ, Jung SM, Kim BJ, Yoon TS, Kim YS, Lee HH (2010) Characterization of Charging Effect of Citrate-Capped AuNP Pentacene Device. J. ind. eng. chem. 16: 848-851.

[8] Xu SP, Zhao B, Xu WQ, Fan YG (2005) Preparation of Au-Ag Coreshell Nanoparticles and Application of Bimetallic Sandwich in SERS. Colloid surf. A 257-258: 313-317.

[9] Sánchez-López JC, Abad MD, Kolodziejczyk L, Guerrero E, Fernández A (2011) Surface-Modified Pd and Au NPs for Anti-Wear Applications. Tribol. int. 44: 720-726.

[10] Seino S, Kinoshita T, Otome Y, Maki T, Nakagawa T, Okitsu K, Mizukoshi Y, Nakayama T, Sekino T, Niihara K, Yamamoto TA (2004) Gamma-Ray Synthesis of Composite Nanoparticles of Noble Metals and Iron Oxides. Scripta mater. 51: 467-472.

[11] Kan CX, Zhu XG, Wang GH (2006) Single-Crystalline Gold Microplates: Synthesis, Characterization, and Thermal Stability. J. phys. chem. B 110: 4651-4656.

[12] Liu HB, Ascencio JA, Perez-Alvarez M, Yacaman MJ (2001) Melting Behavior of Nanometer Sized Gold Isomers. J. surf. sci. 491: 88-98.

[13] Siegel J, Lyutakov O, Rybka V, Kolská Z, Švorčík V (2011) Properties of Gold Nanostructures Sputtered on Glass. Nanoscale res. lett. 6: 96.

[14] Švorčík V, Siegel J, Šutta P, Mistrík J, Janíček P, Worsch P, Kolská Z (2011) Annealing of Gold Nanostructures Sputtered on Glass Substrate. Appl. phys. A 102: 605-610.

[15] Solliard C, Flueli M (1985) Surface Stress and Size Effect on the Lattice-Parameter in Small Particles of Gold and Platinium. Surf. sci. 156: 487-494.

[16] Švorčík V, Kvítek O, Lyutakov O, Siegel J, Kolská Z (2011) Annealing of Sputtered Gold Nano-Structures. Appl. phys. A 102: 747-751.

[17] Heo DN, Yang DH, Moon HJ, Lee JB, Bae MS, Lee SC, Lee WJ, Sun IC, Kwon IK (2012) Gold Nanoparticles Surface-Functionalized with Paclitaxel Drug and Biotin Receptor as Theranostic Agents for Cancer Therapy. Biomaterials 33: 856-866.

[18] Lee S, Chon H, Yoon SY, Lee EK, Chang SI, Lim DW, Choo J (2012) Fabrication of SERS-Fluorescence Dual Modal Nanoprobes and Application to Multiplex Cancer Cell Imaging. Nanoscale 4: 124-129.

[19] Choi KY, Liu G, Lee S, Chen XY (2012) Theranostic Nanoplatforms for Simultaneous Cancer Imaging and Therapy: Current Approaches and Future Perspectives. Nanoscale 4: 330-342.
[20] Curry AC, Crow M, Wax A. (2008) Molecular Imaging of Epidermal Growth Factor Receptor in Live Cells with Refractive Index Sensitivity Using Dark-Field Microspectroscopy and Immunotargeted Nanoparticles. J. biomed. opt. 13: 014022.
[21] Švorčík V, Kolská Z, Kvítek O, Siegel J, Řezníčková A, Řezanka P, Záruba K (2011) "Soft and Rigid" Dithiols and Au Nanoparticles Grafting on Plasma-Treated Polyethyleneterephthalate. Nanoscale res. lett. 6: 607.
[22] Švorčík V, Chaloupka A, Záruba K, Král V, Bláhová O, Macková A, Hnatowicz V (2009) Deposition of Gold Nano-Particles and Nano-Layers on Polyethylene Modified by Plasma Discharge and Chemical Treatment. Nucl. instrum. meth. B 267: 2484-2488.
[23] Wang ZL (2000) Characterizing the Structure and Properties of Individual Wire-Like Nanoentities. Adv. mater. 12: 1295-1298.
[24] Hu JT, Odom TW, Lieber ChM (1999) Chemistry and Physics in One Dimension: Synthesis and Properties of Nanowires and Nanotubes. Acc. chem. res. 32: 435-445.
[25] Hollensteiner S, Spiecker E, Dieker C, Jäger W, Adelung R, Kipp L, Skibowski M (2003) Self-Assembled Nanowire Formation During Cu Deposition on Atomically Flat Vse(2) Surfaces Studied by Microscopic Methods. Mater. sci. eng. C 23: 171-179.
[26] Milenkovic S, Nakayama T, Rohwerder M, Hassel AW (2008) Structural characterisation of gold nanowire arrays. J. cryst. growth 311: 194-199.
[27] Lide DR (1994) The Handbook of Chemistry and Physics 74th edn. Boca Raton: Chemical Rubber Company. 68 p.
[28] Greenwood NN (1984) Earnshaw A Chemistry of the Element. New York: Pergamon. 126 p.
[29] Kouklin NA, Kim WE, Lazareck AD, Xu JM (2005) Carbon Nanotube Probes for Single-Cell Experimentation and Assays. Appl. phys. lett. 87: 173901.
[30] Obataya I, Nakamura C, Han S, Nakamura N, Miyake J (2005) Nanoscale Operation of a Living Cell Using an AFM with a Nanoneedle. Nano lett. 5: 27-30.
[31] Gross GW, Wen WY, Lin JW (1985) Transparent I Electrode Patterns for Extracellular, Multisite Recording in Neuronal Cultures. J. neurosci. meth. 15: 243-252.
[32] Pine J (1980) Recording Action-Potentials from Cultured Neurons with Extracellular Micro-Circuit Electrodes. J. neurosci. meth. 2: 19-31.
[33] Švorčík V, Kasálková N, Slepička P, Záruba K, Bačáková L, Pařízek M, Lisa V, Ruml T, Macková A (2009) Cytocompatibility of Ar(+) Plasma Treated and Au Nanoparticle-Grafted PE. Nucl. instrum. meth. B 267: 1904-1910.
[34] Chithrani BD, Ghazani AA, Chan WCW (2006) Determining the Size and Shape Dependence of AuNP Uptake into Mammalian Cells. Nano lett. 6: 662-668.
[35] Rosi NL, Giljohann DA, Thaxton CS, Lytton-Jean AKR, Han MS, Mirkin CA (2006) Oligonucleotide-Modified Gold Nanoparticles for Intracellular Gene Regulation. Science 312: 1027-1030.
[36] Favier F, Walter EC, Zach MP, Benter T, Penner RM (2001) Hydrogen Sensors and Switches from Electrodeposited Pd Mesowire Arrays. Science 293: 2227-2231.

[37] Wan Q, Li QH, Chen YJ, Wang TH, He XL, Li JP, Lin CL (2004) Fabrication and Ethanol Sensing Characteristics of ZnO Nanowire Sensors. Appl. phys. lett. 84: 3654-3656.
[38] Yang F, Taggart DK, Penner RM (2009) Fast, Sensitive Hydrogen Gas Detection Using Single Palladium Nanowires That Resist Fracture. Nano lett. 9: 2177-2182.
[39] He B, Morrow TJ, Keating CD (2008) Nanowire Sensors for Multiplexed Detection of Biomolecules. Curr. opin. chem. biol. 12: 522-528.
[40] Cui Y, Wei QQ, Park HK, Lieber CM (2001) Nanowire Nanosensors for Highly Sensitive and Selective Detection of Biological and Chemical Species. Science 293: 1289-1292.
[41] Poborchii VV, Tada T, Kanayama T (2002) Photonic-Band-Gap Properties of Two-Dimensional Lattices of Si Nanopillars. J. appl. phys. 91: 3299-3305.
[42] Au FCK, Wong KW, Tang YH, Zhang YF, Bello I, Lee ST (1999) Electron Field Emission from Silicon Nanowires. Appl. phys. lett. 75: 1700-1702.
[43] Gotschy W, Vonmetz K, Lietner A, Aussenegg FR (1996) Thin Films by Regular Patterns of Metal Nanoparticles: Tailoring the Optical Properties by Nanodesign. Appl. phys. B 63: 381-384.
[44] Oates TWH, Keller A, Facsko S, Mücklich A (2007) Aligned Silver Nanoparticles on Rippled Si Templates with Anisotropic Plasmon Absorption. Plasmonics 2: 47-50.
[45] Busbee BD, Obare SO, Murphy CJ (2003) An Improved Synthesis of High-Aspect-Ratio Gold Nanorods. Adv. mater. 15: 414-416.
[46] Zhang XY, Zhang LD, Lei Y, Zhao LX, Mao YQ (2001) Fabrication and Characterization of Highly Ordered Au Nanowire Arrays. J. mater. chem. 11: 1732-1734.
[47] Mbindyo JKN, Mallouk TE, Mattzela JB, Kratochvilova I, Razavi B, Jackson TN, Mayer TS (2002) Template Synthesis of Metal Nanowires Containing Monolayer Molecular Junctions. J. am. chem. soc. 124: 4020-4026.
[48] Wirtz M, Martin CR (2003) Template-Fabricated Gold Nanowires and Nanotubes. Adv. mater. 15: 455-458.
[49] Ghanem MA, Bartlett PN, De Groot P, Zhokov A (2004) A Double Templated Electrodeposition Method for the Fabrication of Arrays of Metal Nanodots. Electrochem. commun. 6: 447-453.
[50] Švorčík V, Slepička P, Švorčíková J, Špírková M, Zehentner J, Hnatowicz V (2006) Characterization of Evaporated and Sputtered Thin Au Layers on Poly(Ethylene Terephtalate). J. appl. polym. sci. 99: 1698-1704.
[51] Kaune G, Ruderer MA, Metwalli E, Wang W, Couet S, Schlage K, Röhlsberger R, Roth SV, Müller-Buschbaum P (2009) In Situ GISAXS Study of Gold Film Growth on Conducting Polymer Films. Appl. mater. interf. 1: 353-362.
[52] Kolská Z, Švorčík V, Siegel J (2010) Size-Dependent Density of Gold Nano-Clusters and Nano-Layers Deposited on Solid Surface. Collect. czech. chem. C. 75: 517-525.
[53] Donor-Mor I, Barkay Z, Filip-Granit N, Vaskevich A, Rubinstein I (2004) Ultrathin gold island films on silanized glass. Morphology and optical properties. 16:3476-3483.
[54] Haupl K, Lang M, Wissmann P (1986) X-Ray-Diffraction Investigations on Ultra-Thin Gold-Films. Surf. interface anal. 9: 27-30.

[55] Shyjumon I, Gopinadhan M, Ivanova O, Quaas M, Wulff H, Helm CA, Hippler R (2006) Structural Deformation, Melting Point and Lattice Parameter Studies of Size Selected Silver Clusters. Eur. phys. j. D37: 409-415.
[56] Santos VL, Lee D, Seo J, Leon FL, Bustamante DA, Suzuki S, Majima Y, Mitrelias T, Ionescu A, Barnes CHW (2009) Crystallization and Morphology of Au/SiO(2) Thin Films Following Furnace and Flame Annealing. Surf. sci. 603: 2978-2975.
[57] Tauc J (1974) Amorphous and Liquid Semiconductors. Heidelberg: Springer. 202 p.
[58] Fischer W, Geiger H, Rudolf P, Wissmann P (1977) Structure Investigations on Single-Crystal Gold-Films. Appl. phys. 13: 245-253.
[59] Slepička P, Kolská Z, Náhlík J, HnatowiczV, Švorčík V (2009) Properties of Au Nanolayers on PET and PTFE. Surf. interface anal. 41: 741-745.
[60] Hovel M, Gompf B, Dressel M (2010) Dielectric Properties of Ultrathin Metal Films Around the Percolation Threshold. Phys. rev. B 81: 035402.
[61] Hodgman CD (1975) Handbook of Chemistry. Cleveland: Chemical Rubber. 264 p.
[62] Chopra K (1969) Thin Film Phenomena. New York: Wiley. 138 p.
[63] Siegel J, Krajcar R, Kolská Z, Hnatowicz V, Švorčík V (2011) Annealing of Gold Nanostrucutres Sputtered on Polytetrafluoroethylene. Nanoscale res. lett. 6:588.
[64] Švorčík V, Kotál V, Siegel J, Sajdl P, Macková A, Hnatowicz V (2007) Ablation and Water Etching of PE Modified by Ar Plasma. Polym. degrad. stabil. 92: 1645-1649.
[65] Siegel J, Řezníčková A, Chaloupka A, Slepička P, Švorčík V (2008) Ablation and water etching of plasma-treated polymers. Radiat. eff. deffect S 163: 779-788.
[66] Švorčík V, Řezníčková A, Kolská Z, Slepička P (2010) Variable Surface Properties of PTFE Foils. e-Polymers 133: 1-6.
[67] Siegel J, Slepička P, Heitz J, Kolská Z, Sajdl P, Švorčík V (2010) Gold Nano-Wires and Nano-Layers at Laser-Induced NanoRipples on PET. Appl. surf. sci. 256: 2205-2209.
[68] Bäuerle D (2000) Laser Processing and Chemistry. Berlin-Heidelberg-New York: Springer-Verlag. 378 p.
[69] Dunn DS, Ouderkirk AJ (1990) Chemical and Physical Properties of Laser-modified Polymers. Macrolmolecules 23:770-774.
[70] Siegel J, Heitz J, Švorčík V (2011) Self-organized Gold Nanostructures on Laser Patterned PET. Surf. coat. technol. 206:517-521.